Title	Numerical modeling of fast electron generation in the presence of preformed plasma in laser-matter interaction at relativistic intensities
Author(s)	Paradkar, B. S.; Wei, M. S.; Yabuuchi, T. et al.
Citation	Physical Review E. 2011, 83(4), p. 046401
Version Type	VoR
URL	https://hdl.handle.net/11094/3447
rights	Paradkar, B. S., Wei, M. S., Yabuuchi, T., Stephens, R. B., Haines, M. G., Krasheninnikov, S. I., Beg, F. N., Physical Review E, 83, 4, 046401, 2011-04-04. "Copyright 2011 by the American Physical Society."
Note	

PHYSICAL REVIEW E **83**, 046401 (2011)

Numerical modeling of fast electron generation in the presence of preformed plasma in laser-matter interaction at relativistic intensities

B. S. Paradkar,[1] M. S. Wei,[2] T. Yabuuchi,[1] R. B. Stephens,[2] M. G. Haines,[3] S. I. Krasheninnikov,[1] and F. N. Beg[1]
[1] *University of California-San Diego, La Jolla, California, 92093, USA*
[2] *General Atomics, San Diego, California, 92186, USA*
[3] *Physics Department, Imperial College, London, SW7 2AZ, United Kingdom*

(Received 5 December 2010; published 4 April 2011)

Fast electron generation in the presence of coronal plasma in front of a solid target (typically referred to as preformed plasma) in laser-matter interaction in the intensity range of 10^{19}–10^{21} W/cm^2 is studied in a one-dimensional slab approximation with particle-in-cell (PIC) simulations. Three different preformed plasma density scale lengths of 1, 5, and 15 μm are considered. We report an increase in both mean and maximum energy of generated fast electrons with an increase in the preformed plasma scale length (in the range 1–15 μm). The heating of plasma electrons is predominantly due to their stochastic motion in counterpropagating electromagnetic (EM) waves (incident and reflected waves) and the presence of a longitudinal electric field produced self-consistently inside the preformed plasma. The synergetic effects of this longitudinal electric field and EM waves responsible for the efficient preformed plasma electrons heating are discussed.

DOI: 10.1103/PhysRevE.83.046401 PACS number(s): 52.57.Kk, 52.65.Pp

I. INTRODUCTION

Laser-matter interaction at relativistic intensities ($I_{\rm laser} > 10^{18}$ W/cm^2) has been a topic of immense interest and extensive investigation, both experimentally and theoretically, due to its significant effects on a number of applications, including fast ignition, [1] electron-ion acceleration, [2,3] electron-positron pair production, [4] etc. One topic that has attracted considerable attention is the role of preformed plasma, produced by intrinsic laser prepulse (i.e., nanosecond pedestal) on laser-matter interactions and its subsequent effect on fast electron generation and transport. This preformed plasma density scale length could be as high as 15–20 μm (in planar targets) for a typical energy contrast of 10^{-5} between the prepulse and energetic main pulses of energies 10–100 kJ. Even in the case of a laser system with a high-energy contrast ratio ($\sim 10^{-8}$), considerable plasma can be expected to build up in front of a dense target due to plasma expansion for a relatively long-pulse ($\sim$20 ps), high-intensity, high-power laser, especially in the relevant fast ignition experiments. Therefore, the interaction of the short-pulse laser with preformed plasma is inevitable in laser-solid interaction experiments, particularly with 1-μm lasers.

The problem of the fast electron generation due to the relativistic intensity laser absorption in such preformed plasma has been addressed in a number of experimental and theoretical studies. Typically, laser-plasma interaction (LPI) generated fast electrons are characterized by the slope temperature $T_{\rm hot}$ of their energy spectrum. The two scalings most widely used for the mean energies ($T_{\rm hot}$) of fast electrons are the experimentally determined Beg's scaling [5] or Wilks' numerically modeled ponderomotive scaling [6]. These scalings do not address the dependence of $T_{\rm hot}$ on finite-scale-length preformed plasma in front of the target. However, the recent experiments [7,8] and numerical modeling [9–11] have suggested that the presence of preformed plasma can significantly affect the fast electron energy distribution. In general, these studies have reported an increase in the fast electrons' mean energy with increasing preformed plasma scale length. Similar trends were also observed in the particle-in-cell (PIC) simulations [12,13] performed for the intensities of the order of 10^{19} W/cm^2. However, the physics of such increases in the fast electron energy with increasing preformed plasma is still not well understood. Also, to the best of our knowledge, preformed plasma scale length effects on fast electron generation over the wide intensity range of 10^{19}–10^{21} W/cm^2 have not been systematically studied.

In the present work, we address this problem with a systematic numerical study of LPI at relativistic intensities achievable with present day laser technology (i.e., from 10^{19} to 10^{21} W/cm^2) for various preformed plasma scale lengths typically expected in the experiments (i.e., from 1 to 15 μm). We have studied the dynamics of fast electron generation due to the interaction of a short pulse laser with preformed plasma in a one-dimensional (1D) slab approximation with 1D three-velocity (1D3V) PIC simulations for three preformed plasma scale lengths of 1, 5, and 15 μm. The choice of a simplified 1D approximation, because it is computationally cheap, allows us to simulate the LPI over a wide range of preformed plasma scale lengths and laser intensities. The simulations are performed with both mobile and immobile ion assumption. In the majority of our simulations, the ions are considered to be immobile in order to keep the interaction independent of solid target material. The effect of ion mobility and ponderomotive steepening of the plasma density profile [9] is studied by performing separate simulations for the case of fully ionized aluminum. The multidimensional effects of LPI such as laser self-focusing [14] and filamentation [15] may play a role in the experiments. However, these effects are neglected in the present work for simplicity.

This paper is arranged as follows: The details of numerical modeling and simulation results are given in Sec. II. The electron dynamics caused by the synergetic effects of the electromagnetic (EM) waves and longitudinal electric field are discussed in Secs. III and IV with the help of PIC simulations. Section V addresses the effect of ion mobility on fast electron production. Final conclusions are given in Sec. VI.

II. THE RESULTS OF PIC MODELING WITH IMMOBILE IONS

The simulations are performed with the PIC code, Large Scale Plasma (LSP) [16,17], used in 1D3V phase space. LSP, being an implicit PIC code, allows the use of the grid resolution greater than the Debye length without causing excess numerical heating. This feature makes it suitable for simulating laser-solid interactions at relativistic intensities. For example, the Debye length for plasma at a density of 10^{23} cm^{-3} and 5 keV electron temperature is $\sim 1.6 \times 10^{-3}$ μm. LSP relaxes the stringent computational requirement of resolving such small spatial scales. A spatial resolution of 80 cells per laser wavelength ($=1$ μm) with 300 particles per cell is used in the simulations. The cell size, $\Delta_x = 1.25 \times 10^{-2}$ μm, ensures that the collisionless skin depth and lowest preplasma scale length (1 μm) are well resolved. The time step $c\Delta t = 10^{-3}$ μm is chosen to satisfy the Courant stability criterion [17]. The initial plasma density profile is taken as [11]

$$n_e x = \frac{Z n_{\text{solid}}}{1 + \exp[-2(x - x_0)/L_p]}, \tag{1}$$

where L_p denotes the preformed plasma scale length, Z is the ion charge state, and n_{solid} is the solid ion density. Simulations are run with preformed plasma scale lengths of 1, 5, and 15 μm. Fully ionized aluminum plasma with an initial temperature of 5 keV is used in the simulations. The selection of aluminum would only affect mobile ion simulation results through its ion inertia. Of course, the implicit assumption here is that the slow ion motion can be neglected on the time scales of fast motion of electrons in the laser field and ion motion would affect the LPI only through the modification of the preformed plasma profile. The linearly polarized laser enters the simulation box from the left boundary (Fig. 1) with the laser pulse reaching maximum intensity in ten laser cycles (i.e., 33 fs). The simulations are run with three different laser intensities of 10^{19}, 10^{20}, and 10^{21} W/cm^2. The direction of laser propagation is defined as the X direction, whereas the laser electric and magnetic fields are pointed in the Z and Y directions, respectively. The fast electron energy spectrum is obtained by analyzing the electrons behind the relativistic critical density surface (inside the counting box B as shown by dotted lines in Fig. 1). Figure 1(b) shows the temporal variation of Poynting flux through plane AA' for the case of $I = 10^{20}$ W/cm^2. The quasisteady state of the simulation is defined as the time when the laser net forward energy flux becomes approximately constant and equal to the particle energy flux entering the solid target. The estimate of the fast electrons' mean energy based on electron distribution functions is obtained when this quasisteady state is reached. For example, in Fig. 1(b), a quasisteady state is reached after $\sim$400 fs. Fast electron refluxing [18] from the back of the target is avoided by choosing longer target dimensions. Therefore, results presented in this paper are valid under the thick target approximation with no refluxing of electrons from a foil's rear surface into the LPI region. Such electron refluxing could significantly modify these simulations [18].

One issue that is critically important in high-intensity laser-matter interaction is to correctly characterize the fast electrons' energy spectrum. In general, the most important quantity of interest is the mean energy (E_{mean}) of generated fast electrons going into the target. Typically this quantity is determined by fitting the electron distribution function, $f(E)$ [shown in Fig. 2(a)] by a function of the form $A_0 \exp(-E/T_{\text{hot}})$, where T_{hot} is called the slope temperature [11]. The electron distribution function $f(E)$ is normalized as

$$n = \int_0^\infty f(E)\,dE, \tag{2}$$

where n is the electron density and E is the kinetic energy of an electron. But this direct correlation between E_{mean} and T_{hot} breaks down when the electron energy spectrum is non-Maxwellian, which is usually the case with high-intensity laser-matter interactions. Therefore, the mean energy of fast electrons obtained from this method is very sensitive to the energy range chosen to fit the spectrum, especially in the

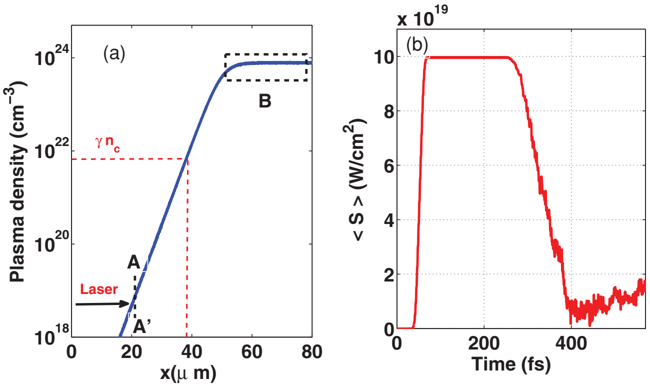

FIG. 1. (Color online) Schematic of simulation setup. The linearly polarized laser enters the simulation box from the left boundary and travels in a $+X$ direction. The laser intensity in this simulation is 10^{20} W/cm^2 whereas preformed plasma scale length is 5 μm. The fast electrons generated by laser-plasma interaction are counted inside the solid inbox B for the analysis of electron energy distribution. Relativistic critical density surface is shown by dotted (red) lines in (a). The temporal variation of laser forward energy flux through plain AA' is shown in (b).

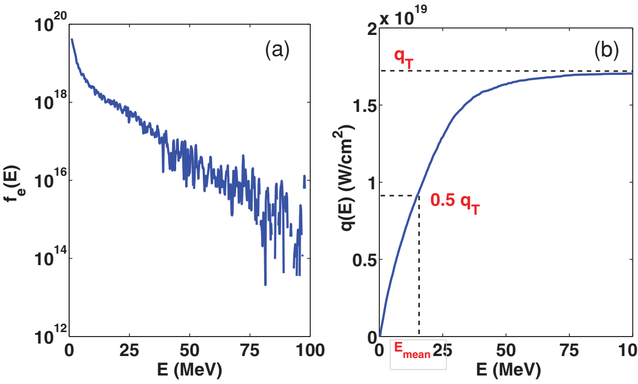

FIG. 2. (Color online) (a) Electron energy distribution inside the target for laser intensity of 10^{20} W/cm^2 and 15 μm preplasma scale length. (b) Cumulative heat flux carried by the electrons inside the target. The mean energy E_{mean} is defined as the energy for which half of the total heat flux q_T is carried by hotter electrons and the other half by colder electrons.

low-energy part of the spectrum [11]. The more meaningful estimate of the fast electron mean energy, especially for fast ignition [1] studies, can be made based on the electron energy flux distribution function or heat flux $w(E)$ defined in the following way:

$$q(E) = \int_0^E w(E)\,dE = \int_0^E f(E)EV_x\,dE, \tag{3}$$

where $q(E)$ is the heat flux carried along the laser propagation direction by the electrons with energies less than E, and V_x is the electron velocity in the laser propagation direction. Thus, the total heat flux q_T carried by the electrons inside the target is given by

$$q_T = \int_0^\infty w(E)\,dE = \int_0^\infty f(E)EV_x\,dE. \tag{4}$$

Now, we define the mean energy E_{mean} of the fast electron spectrum as the energy at which half of the total electron heat flux ($0.5q_T$) is captured. Figure 2(b) illustrates the method of calculating the mean energy used in this paper. This method gives us a direct quantitative estimate of the energy at which the incident laser energy is converted into the fast electron energy without the introduction of any arbitrary lower-energy cutoff, which was used in Ref. [11].

The fast electron energy spectra obtained for the three preformed plasma scale lengths ($L_p = 1$, 5, and 15 μm) at three laser intensities ($I = 10^{19}$, 10^{20}, and 10^{21} W/cm^2) are analyzed by the above-mentioned method. Figure 3(a) shows the fast electron energy spectra at the laser intensity of 10^{20} W/cm^2. The dependence of the mean electron energy on laser intensity and preformed plasma scale length is plotted in Fig. 3(b). It is clear that the longer-scale-length preformed plasma results in the higher mean energy of fast electrons, in agreement with earlier published experimental and numerical work [7–10]. For the long preformed plasma cases (i.e., 5 and 15 μm), the E_{mean} obtained is higher than the laser ponderomotive energy E_p [6] for the corresponding laser intensity. In addition, we also observe that the maximum energy of fast electrons in the spectrum ($E_{\max}$) increases with an increase in the preformed plasma scale length. For example, for the laser intensity of 10^{20} W/cm^2, the mean energies for 1, 5, and 15 μm cases are ~3.1, 6.3, and 14 MeV, respectively, whereas the ponderomotive energy at this intensity is 3.8 MeV. The corresponding maximum energies for these scale lengths are 25, 75, and 100 MeV, respectively.

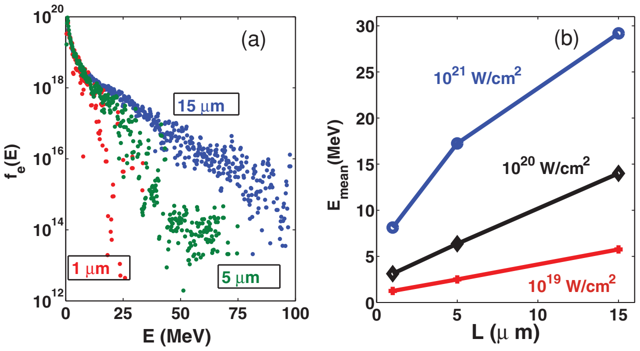

FIG. 3. (Color online) (a) Electron energy distribution inside the target for three preformed plasma scale lengths for a laser intensity of 10^{20} W/cm^2. (b) The mean energy of electrons obtained by the method described in Fig. 2(b) for various preformed plasma scale lengths and intensities. The increase in both the mean and maximum energy with increasing preformed plasma scale lengths is evident from these plots. The ponderomotive energies corresponding to laser intensities 10^{19}, 10^{20}, and 10^{21} W/cm^2 are 0.9, 3.8, and 13 MeV, respectively.

Finally, we performed the χ^2 minimum fitting on the mean energies obtained for the various intensities and preformed plasma scale lengths with a fitting function of the form $E_{\text{mean}} = \kappa I_L^\alpha L_p^\beta$, where I_L and L_p are the laser intensity normalized by 1.37×10^{18} W/cm^2 and the preformed plasma scale length in μm, respectively. This fitting gives E_{mean} as

$$E_{\text{mean}}\,(\text{MeV}) = (0.72 \pm 0.13)\,(I_L)^{0.36\pm0.02}\,(L_P)^{0.5\pm0.06}. \tag{5}$$

Note that the above fitting is obtained for the laser intensity range of 10^{19}–10^{21} W/cm^2 and preformed plasma scale length range of 1–15 μm.

Thus, we find that both the mean and the maximum energies of the generated fast electrons increase with an increase in the preformed plasma scale length. In order to understand the underlying physics of the above-mentioned results, we have analyzed the dynamics of the electrons as the laser starts interacting with the preformed plasma. In the next section, we discuss the dynamics in detail.

III. THE DYNAMICS OF ELECTRONS IN LASER INTERACTION WITH PREFORMED PLASMA (IMMOBILE IONS)

As described above, the mean electron energy and spectra are affected by the preformed plasma scale lengths. Now, the key question is: What is the mechanism of the plasma electrons' heating which leads to such varying spectra with preformed plasma scale lengths? In this section, we will address this question.

The essential feature of electron heating by an EM wave is the phase randomization of electrons in an oscillating field of the wave. This is due to the fact that a single electron oscillating coherently with the electric field of a plane wave gains zero cycle averaged energy since the electron energy gain in one half cycle is exactly equal to the energy loss in the next half cycle. This is generally referred to as the Woodward-Lawson theorem [19]. The various causes of this breaking of phase coherence in LPIs are electron-ion collisions [20], laser ponderomotive force ($\boldsymbol{V} \times \boldsymbol{B}$ force) [21], counterpropagating EM waves [22,23], etc. Especially for the high-intensity short pulse lasers, the $\boldsymbol{J} \times \boldsymbol{B}$ heating [21] and stochastic heating [22,23] by counterpropagating EM waves are considered to be the dominant heating mechanisms. We will investigate the electron heating process by analyzing the electron phase-space (P_x vs X) dynamics at various stages of the interaction.

Figure 4 describes the dynamics of laser interaction with preformed plasma during the initial stages for the case of a laser intensity of 10^{20} W/cm^2 and a preformed plasma scale length of 5 μm. The phase-space density $D(X,P_x)$ shown in Figs. 4(a), 4(c), and 4(e) gives a number proportional to the number of electrons found between X and $X+dX$ having longitudinal momentum in the range $(P_x, P_x + dP_x)$. The normalized electrostatic potential due to the longitudinal electric field E_x

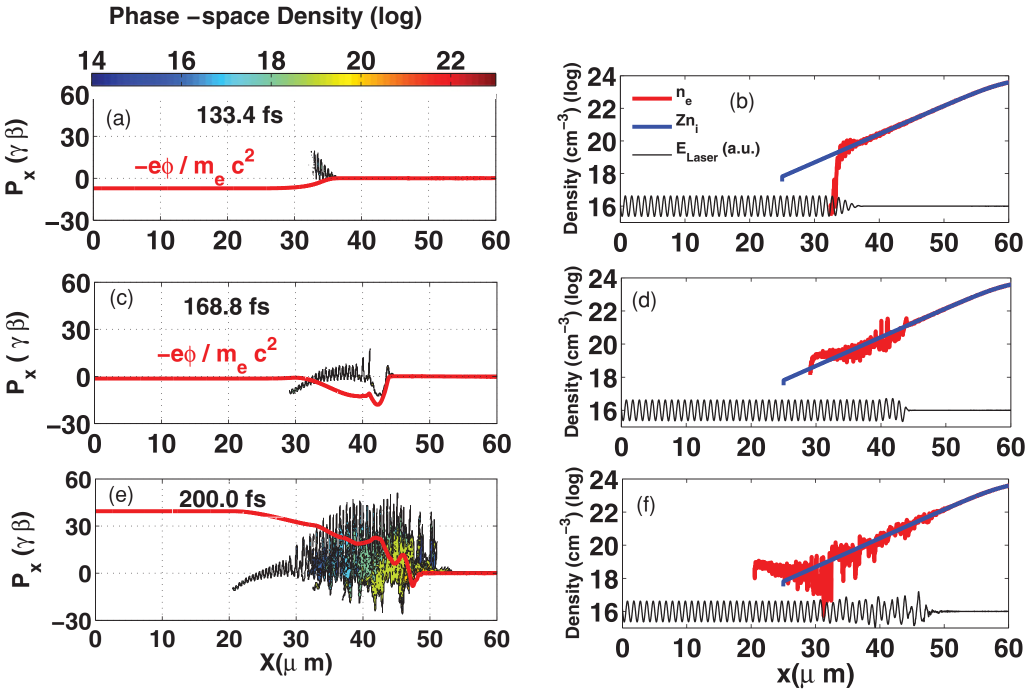

FIG. 4. (Color online) Laser interaction with preformed plasma during initial stages of laser propagation through underdense plasma. (a), (c), and (e) The phase-space density (plotted on color scale) and electrostatic potential due to the longitudinal electric field (solid red line) at times 133.4, 166.8, and 200 fs, respectively. Corresponding electron and ion plasma densities and laser electric fields are plotted in (b), (d), and (f), respectively. Electron phase-space mixing by counterpropagating EM waves can be seen from (e) and (f). Note that mixing occurs only in the region of incident and reflected waves (from 30 to 50 μm). The laser propagates up to 48 μm, as can be seen from (f).

is also shown in the red curve. The electron momentum is plotted in the usual dimensionless units of $\gamma\beta$. Figures 4(b), 4(d), and 4(f) are the electron (red line) and ion (blue line) densities and the laser electric field E_z corresponding to the times shown in Figs. 4(a), 4(c), and 4(e), respectively. In the very early stages of laser propagation through underdense preformed plasma [Figs. 4(a) and 4(b)], all the electrons are swept away in the forward direction ($+X$ direction) by the laser ponderomotive force, leaving behind immobile ions. This forward electron acceleration by the ponderomotive force is evident from 2ω electron oscillations. The electrostatic potential due to charge separation in the underdense plasma tries to pull the electrons in the backward direction. As the laser propagates further toward a critical density surface [Figs. 4(c) and 4(d)], the electrons experience a stronger backward pull due to increasing electrostatic potential. Negative values of momentum in Fig. 4(c) illustrate the backward movement of some of the electrons. Now, the reversal of longitudinal electric field polarity (in the $-X$ direction) in response to this backward movement of electrons can be seen from the potential curve in Fig. 4(c). Finally, we observe the strong phase-space mixing when part of the incident light is reflected back from the relativistic critical density ($\gamma_{\rm osc} n_c$) surface which is present at $\sim$48 μm for this simulation [Figs. 4(e) and 4(f)]. Here, $\gamma_{\rm osc}$ for laser vector potential a_0 is defined as $\gamma_{\rm osc} = \sqrt{1 + a_0^2/2}$. The phase-space mixing occurs in the region (between 30 and 50 μm) where we have two counterpropagating EM waves (incident and reflected laser light). The increase in the electron energy with the disappearance of distinct 2ω oscillations in this region clearly demonstrates the stochastic electron heating [22,23] by these two counterpropagating waves. We also observe strong nonlinear electrostatic plasma waves produced by the laser ponderomotive force, travelling predominantly down the density gradient (against the direction of incident laser propagation, i.e., $-X$ direction) as in the resonance absorption. But the contribution of these waves to electron heating via wave-particle interactions such as Landau damping is found to be insignificant. The peak value of electrostatic potential of these plasma waves is much smaller than the actual energy gain by the electrons seen in the simulations. Therefore, for the laser intensities simulated in this paper, we find that the stochastic heating by counterpropagating EM waves is the dominant mechanism.

As the electrons' heating continues, the stochastic motion of electrons in counterpropagating EM waves leads to the mixing of phase-space fluid. This results in the homogenization of phase-space density in the region of mixing. This physical picture can be easily seen in the later phase-space density plots shown in Fig. 5. The colors in these plots show the local phase-space density. Also, this representation of phase-space density clearly indicates how the electrons' energy spectrum varies with spatial coordinates (e.g., the flow of phase-space fluid). Thus, from Fig. 5 we can infer that the very high-energy tail (shown by the blue color) of the electron distribution inside the target is essentially due to the electrons in the low-density region of the preformed plasma. Here, we would like to emphasize the fact that this phase-space fluid trajectory should not be mistaken as the trajectory of an individual electron

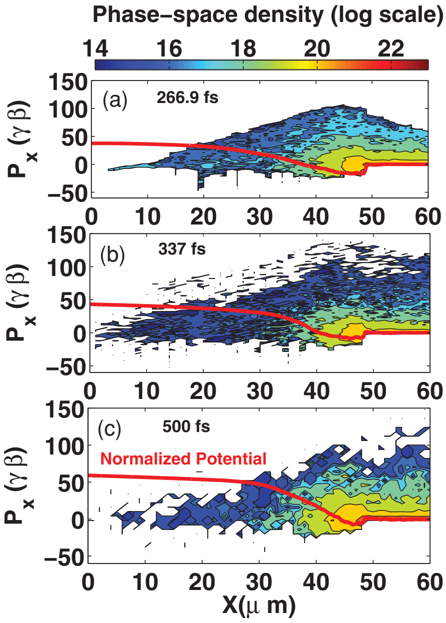

FIG. 5. (Color online) Phase-space density evolution as the laser starts heating the preformed plasma. The colors indicate phase-space density caused by phase-space mixing due to the counterpropagating laser field. The solid red line represents normalized electrostatic potential ($-e\phi/m_ec^2$). The increase in the maximum value of the potential and corresponding decrease in the electron density escaping toward the low-density side demonstrates how plasma confines these electrons.

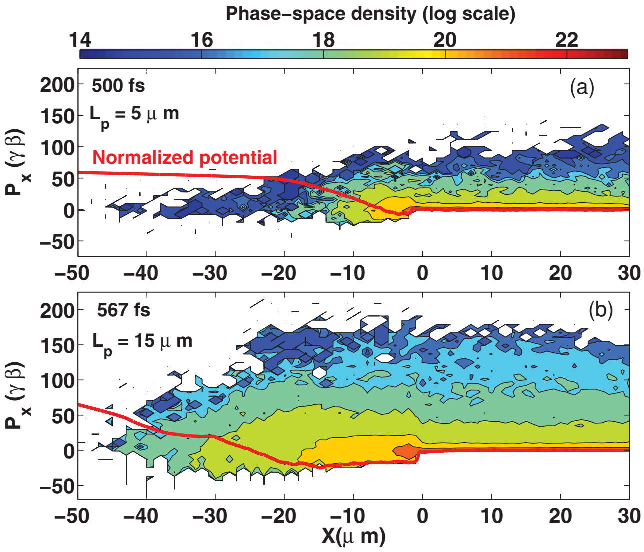

FIG. 6. (Color online) Comparison of phase-space plots for (a) 5 μm and (b) 15 μm preformed plasma scale lengths (laser intensity$=1\times10^{20}$ W/cm^2). Note the extension of the phase-space mixing region (0 to -45 μm) for the case of 15-μm preformed plasma with higher energies compared to 5-μm preplasma. Also, the electrostatic potential well developed in the preformed plasma due to the electron heating is wider for long-scale-length preformed plasma.

in that region of phase space. This is especially true in the phase-space mixing region.

The electron heating near the relativistic critical density surface results in an increase in electron pressure (n_eT_e) in the region of laser absorption. The pressure gradient causes the heated plasma expansion from the absorption region. The electrostatic potential well (solid red line in Fig. 5) self-consistently appears in response to the plasma electrons' expansion from this region. In other words, the plasma electrons' heating causes the setting up of this longitudinal electrostatic potential well to maintain quasineutrality. The progressive increase in the maximum value of potential [from Fig. 5(a) to 5(c)] and a corresponding decrease in the electrons escaping to the lower density side (from 0 to 30 μm, in Fig. 5) demonstrates how plasma potential changes in order to maintain quasineutrality. It should be noted that this potential also brings the cold, fresh electrons from the solid target into the interaction region. The cold electrons finally enter the target as heated electrons. This explains how the quasisteady state is achieved in these simulations (typically in 200–400 fs depending upon the preformed plasma scale length).

With this picture of the preformed plasma electrons' heating in mind, we now try to investigate the differences in the electron energy spectra inside the target for different preformed plasma scale lengths by comparing the quasisteady-state phase-space density plots of different scale lengths (5 and 15 μm) for the same laser intensity of 10^{20} W/cm^2 (Fig. 6). Note that the relativistic critical density surface is defined as $X=0$ in these figures. Clearly, we see an extension of the phase mixing region in the case of a shallower density profile ($L_p=15$ μm) with a wider potential well due to the reduced longitudinal electric field. Here, the electric field is weakened because of the long scale length of the preformed plasma ($E_x\sim T_h/L_p$). The increase in electron energy for the same phase-space density [shown by the same colors found in Figs. 6(a) and 6(b)] indicates the increase in mean energy in the case of long-scale-length preformed plasma compared to the short-scale-length preformed plasma. Also, the maximum energy of electrons seen inside the target is greater for the 15-μm scale length case. Thus, these observations are consistent with the results reported in Sec. II. From this we conclude that the extension of the phase-space mixing region in the presence of a wider potential well leads to higher mean and maximum fast electron energies for the case of long-scale preformed plasma. In addition, we observe that the mean energies for these two cases are higher than the ponderomotive energy E_p at the given laser intensity (Fig. 3). For example, for laser intensity 10^{20} W/cm^2, E_p is 3.8 MeV whereas mean energies for 5 and 15 μm are 6.37 and 17.25 MeV, respectively. These results indicate that the electron heating process is strongly influenced by this longitudinal electrostatic potential well.

In order to investigate the exact physics behind this increase in electron energies in the presence of long-scale preformed plasma with mean energies greater than ponderomotive energy, we performed a separate set of simulations with counterpropagating EM waves with and without the electrostatic potential well. Note that the counterpropagating EM waves and electrostatic potential well associated with the expansion of heated plasma electrons are found to be essential features of the LPI for all the preformed plasma scale lengths. The width

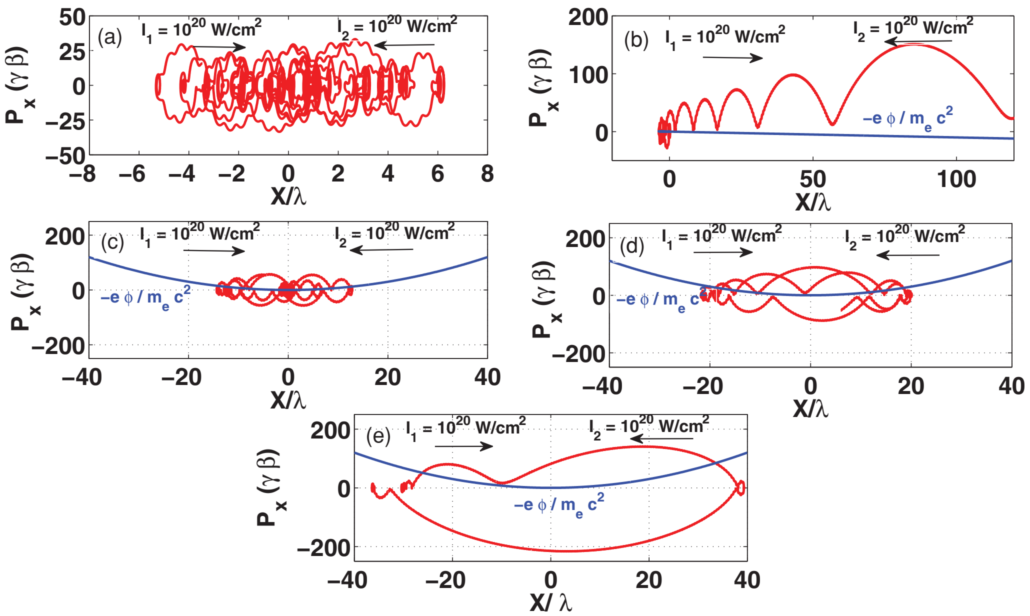

FIG. 7. (Color online) Single electron phase-space trajectories with counterpropagating EM waves and longitudinal electric field. (a) Stochastic electron motion without longitudinal electric field. (b) The electron motion in the presence of a constant longitudinal electric field. The electron, once detrapped due to the constant push of electric field, continues to move with the forward-going wave. This is defined as locking with the forward wave. (c), (d), (e) The electron dynamics in the presence of quadratic potential well (shown by blue line) for the electron initial positions of 0, −20, and −30, respectively. The electron, starting higher up in the potential (e), gains more energy due to locking with either of the waves.

and the depth of this well are decided by various factors such as plasma heating, preformed plasma scale length, ion mobility (this will be demonstrated in Sec. V), etc. The numerical setup, results, and physics of electron heating in the presence of a potential well are discussed in the next section.

IV. THE SYNERGETIC EFFECTS OF COUNTERPROPAGATING EM WAVES AND ELECTROSTATIC POTENTIAL WELL ON THE DYNAMIC OF ELECTRONS

The phase-space dynamics in counterpropagating EM waves with or without the presence of an electrostatic potential well can be clearly understood by first analyzing the motion of a single electron in such a field. We have studied such motion by numerically solving the 1D3V electron equation of motion with the standard Boris algorithm [24]. Figure 7 shows the phase-space trajectories of a single electron under various conditions. The intensity of both the counterpropagating linearly polarized EM waves is taken as 10^{20} W/cm^2. Figure 7(a) shows the trajectory of the electron in the absence of a longitudinal electric field. The characteristic features of electron motion, consisting of trapping (shrinking of phase-space area, i.e., adiabatic invariant) and detrapping of the electron are clearly evident from this figure. The maximum normalized longitudinal momentum seen is ∼30. Next, in Fig. 7(b), we introduce a constant longitudinal electric field (i.e., linearly increasing the normalized potential represented by the blue line) in addition to these counterpropagating EM waves. Because of the constant electric field, which pushes the electron continuously in $+X$ direction in this case, the phase slippage of the electron with respect to the forward propagating wave is reduced and therefore the electron starts moving with the forward propagating ($+X$) EM wave. We define this process as electron locking with the forward wave. Note that the energy gain of the electron is much greater than the electrostatic potential. Thus, the longitudinal electric field helps in reducing the phase slippage of an electron with respect to one of the EM waves, thereby causing the nonlinear increase in energy of the electron due to locking with that wave. In the next three cases [Figs. 7(c)–7(e)], we analyze electron motion for different initial positions (at $t = 0$) in a quadratic electrostatic potential well (shown by the blue line). These cases mimic the situations in the actual simulations described in the previous section. In each of these cases the electron starts from rest with the initial positions [$X = 0$, −20, −30 μm for Figs. 7(c), 7(d), and 7(e), respectively]. From Figs. 7(c)–7(e), we see that the electron, once detrapped, oscillates in the potential well by getting locked alternately with the forward and backward EM wave. During this process the electron also gains energy continuously, thereby climbing up the potential during each cycle of forward and backward motion. This feature is clear from Fig. 7(e) where the electron starts from $X = -30$ μm, but after one cycle of oscillation climbs up in the potential to $X = -35$ μm. Also, note the increase in the maximum energy of the electron, as it starts from a region of stronger electric field. The stronger electric field acts as a moderator in reducing the phase slip of the electron with respect to the EM wave, thereby causing higher acceleration due to increased locking distance with either wave. This is consistent with the results in actual simulations where the maximum energy component of the spectrum inside the target comes from the electrons accelerated from the underdense plasma, which is also a region of higher electrostatic potential (Fig. 6). Also,

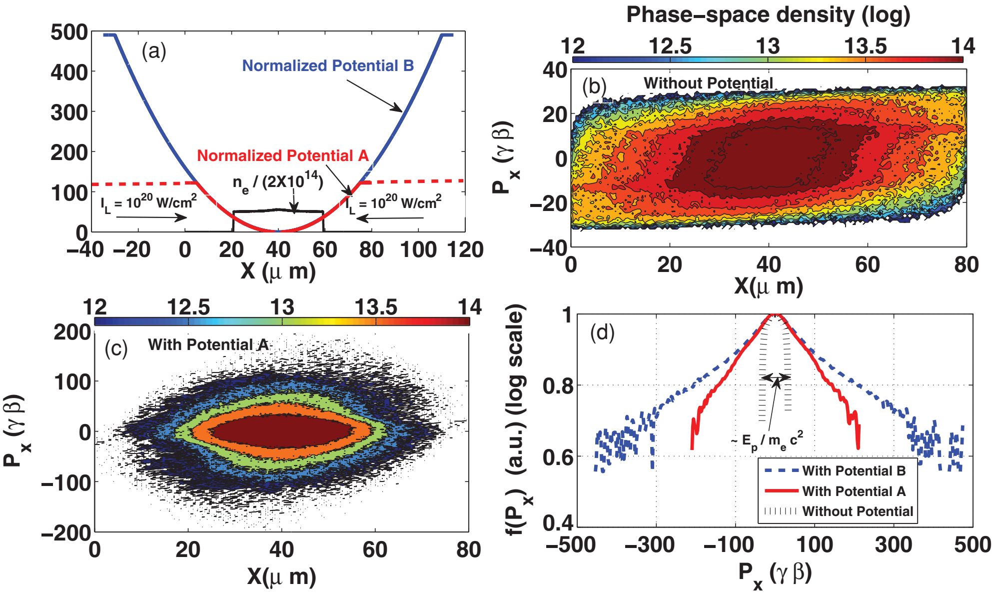

FIG. 8. (Color online) Dynamics of plasma heating due to counterpropagating EM waves with and without potential well. (a) Numerical set of the simulation. (b), (c) Phase-space density plot for the cases with and without potential well A, respectively. Note the increase in maximum energy gained by an electron as it starts from the region of higher electrostatic potential. (d) Comparison of momentum distribution function for cases with (blue and red curve) and without (black curve) potential well. Both the mean and maximum energy of the distribution increases with the potential well, consistent with observations in the actual preplasma scale length simulations discussed in the earlier section.

large preformed plasma allows longer acceleration length to these electrons locked with the forward wave, thereby resulting in an increase in the maximum energy. Keeping the single particle dynamics in mind, it is now easy to interpret the results of the PIC simulations performed to explain plasma heating in two counterpropagating EM waves with and without an electrostatic potential well.

The numerical setup and results demonstrating plasma heating due to counterpropagating EM waves in a potential well (at steady state) are shown in Fig. 8. The two linearly polarized EM waves with equal intensity of 10^{20} W/cm^2 enter the simulation box from the left and right boundaries [Fig. 8(a)]. The plasma density in these simulations is 10^{16} cm^{-3}. This extremely low value of plasma density ensures that the self-consistently excited longitudinal electric fields (including plasma waves) are negligible, and plasma heating is entirely due to the counterpropagating EM waves and the externally imposed electrostatic potential well. As can be seen from Fig. 8(a), simulations are run for two different potentials [potential A (red curve) and potential B (blue curve)]. We also performed a simulation without the potential well for comparison. The phase-space densities for the cases without potential [Fig. 8(b)] and with potential A [Fig. 8(c)] clearly show the increase in electron energies in the presence of the potential well. Note the different P_X range for the Y axis in Figs. 8(b) and 8(c). The comparison of electron momentum distribution is given in Fig. 8(d). For the no-electrostatic-potential case [black curve in Fig. 8(d)], we find that the full width of the distribution is approximately twice the normalized ponderomotive potential ($\sim$3.8 MeV). The phase-space trajectory of a single electron in counterpropagating EM waves, shown in Fig. 7(a), is consistent with the phase-space density plot of Fig. 8(b). Also, the maximum energy obtained ($\gamma \sim 30$) is consistent in both these simulations. On the other hand, the simulations with a potential well show a larger width of the momentum distribution function [blue and red curve in Fig. 8(d)], indicating a higher mean energy. Also, note that increasing the width and depth of the potential well results in an increase in the electron mean energies. The maximum energy with a potential well is also significantly larger than the case without a potential well. Both these results are consistent with the actual preformed plasma scale length simulation results reported in the previous section. The concentric islandlike structures with increasing width along both P_x and X axes seen in the phase-space density plot [Fig. 8(c)] are due to the increase in energy gain by an electron due to the larger locking distance with either of the waves in the presence of a longitudinal electric field. Again, this trend is clear from the single particle dynamics explained in Figs. 7(c)–7(e).

Thus we can explain the plasma heating mechanism for the counterpropagating EM waves in the presence of an electrostatic potential well. The higher mean and maximum energies seen with the longer preformed plasma scale length can also be explained with this heating mechanism. The larger potential well in the case of long-scale-length preformed plasma results in the extension of the phase-space mixing region, thereby causing an increase in the mean energy with an increase in the preformed plasma scale length. The higher maximum energy is essentially due to the longer locking distance with the forward-going wave. The longitudinal electric field plays the role of moderator in locking an electron with one of the EM waves by reducing the phase slippage of the electron with that wave. Finally, we apply this physical picture to the simulations

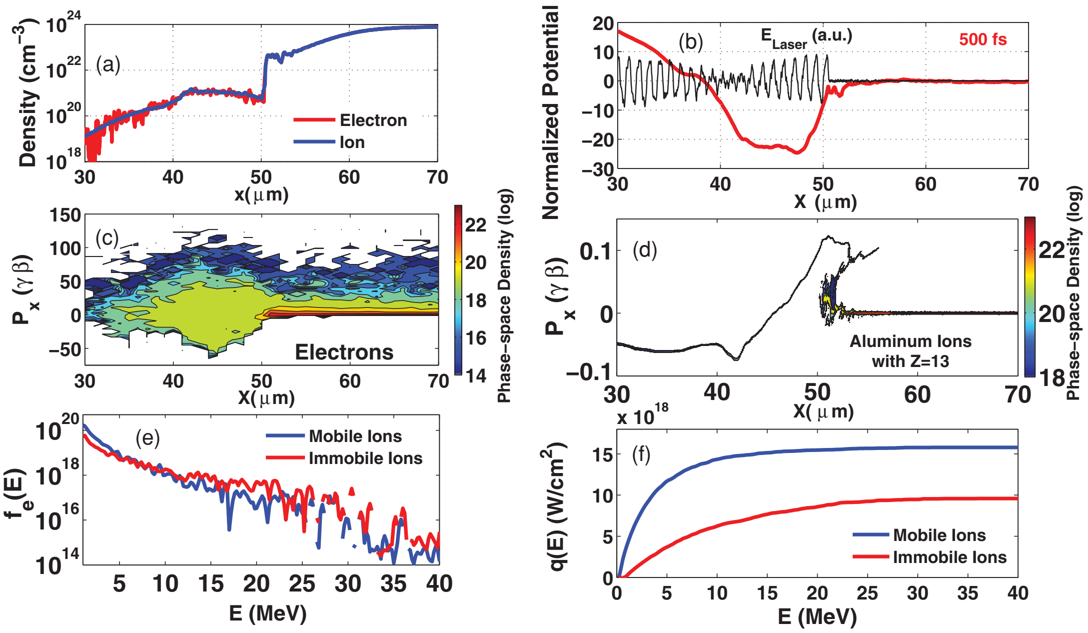

FIG. 9. (Color online) Dynamics with mobile ions ($L_p = 5$ μm; $I_L = 10^{20}$W/cm^2). (a) Electron (red line) and ion (blue line) densities. The density steepening and low-density plasma shelf in front of the relativistic critical density surface can be seen here. (b) Electrostatic potential well (red line) and laser electric field (black line). (c), (d) The electron and ion phase-space density plots. (e) The inside target electron energy distribution function comparison for mobile (blue line) and immobile ion (red line) simulations. (f) The electron cumulative heat flux comparison for mobile (blue line) and immobile ion (red line) simulations.

with mobile ions. The results of mobile ion simulations are discussed in the next section.

V. PIC SIMULATIONS WITH MOBILE IONS

We now turn our attention to the dynamics in the presence of mobile ions. Fully ionized aluminum ($Z = 13$) is chosen for these simulations. The results of the simulation for an initial 5-μm preplasma density scale length and laser intensity of 10^{20} W/cm^2 are shown in Fig. 9. In the case of mobile ion simulations, ions are free to respond to the longitudinal electric field on the time scales decided by the charge to mass (Z/M) ratio of the ion. The steepening of the plasma density profile near the relativistic critical density surface, similar to recently reported results [9], is observed [Fig. 9(a)]. This steepening and the formation of the low-density shelf in front of the relativistic critical density surface can be explained by looking into ion motion [Fig. 9(d)] in the presence of a longitudinal electric field [Fig. 9(b)] induced due to plasma heating and the resulting electron pressure gradient. The ions near the potential minima ($X \sim 45$ μm) are pushed in both $\pm X$ directions, thereby causing a uniform low-density shelf in front of a relativistic critical density surface. Note that the maximum energy of the forward-going ions ($\sim$180 MeV) is consistent with the maximum electrostatic potential ($Ze\varphi$). The density of this lower shelf decreases as it expands towards vacuum. This extension of the low-density shelf toward the vacuum results in the widening of the potential well. Extension of the phase-space mixing region of electrons [Fig. 9(c)] in the preformed plasma due to the wider potential well results in stronger heating of the plasma, which also causes deepening of the potential well due to the increase in plasma electron pressure. The ions are accelerated by the longitudinal electric field caused by the electron pressure gradient. The comparison of mobile ion simulations [Figs. 9(b) and 9(c)] with immobile ions simulations [Fig. 6(a)] clearly demonstrates this mechanism. Naturally, we find higher laser absorption in the case of mobile ion simulations compared to immobile ion simulations. For example, for the initial 5-μm preformed plasma density scale lengths and laser intensity of 10^{20} W/cm^2, we find $\sim$30% absorption with mobile ions compared to 10% absorption with immobile ion simulations. Note that laser absorption is determined from laser Poynting flux as explained in Sec. II (Fig. 1). The comparison of cumulative electron heat flux going into the target is plotted in Fig. 9(f). The electron heat flux for mobile ion simulations (blue line) is 16% whereas it is 10% for immobile ions (red line). Also, note that almost 80% of the total electrons' heat flux is carried by electrons having energy below 5 MeV for mobile ions due to an increase in the number of fast electrons [Fig. 9(e)] in this range.

This trend of increase in the laser absorption with mobile ions continues for other initial preformed plasma scale lengths as well. In Fig. 10 we give laser absorption percentages for various initial preformed plasma scale lengths and laser intensities. In general, we find an increase in the laser absorption with increasing preformed plasma scale lengths, as is the case of immobile ion simulations. This is consistent with the physical picture we have described (i.e., larger phase-space mixing region with longer preformed plasma due to a wider potential well). We would like to note that although we see a significant increase in laser absorption with mobile ions, the underlying physics of this increase for electrons is the same as that of plasma heating due to counterpropagating EM waves and the presence of an electrostatic potential well described

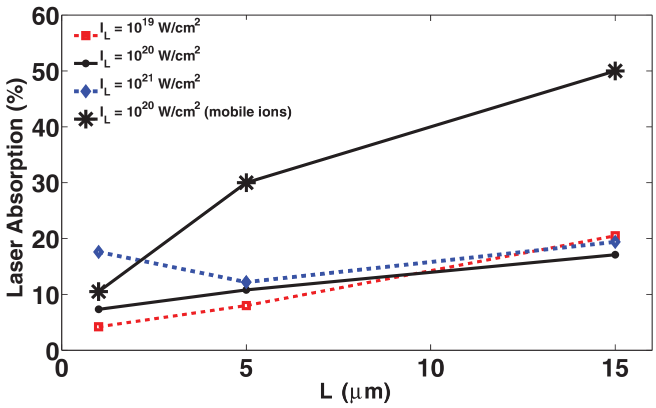

FIG. 10. (Color online) Laser absorption for various initial preformed plasma scale length and laser intensities.

with the help of immobile ion simulations. Also, for the case of a laser with 10^{21} W/cm^2, we observe slightly higher absorption at a scale length of 1 μm as compared to a scale length of 5 μm. A similar trend is reported in the work of Lefebvre *et al.* [13]. We plan to investigate this phenomenon in detail in the future.

VI. CONCLUSION

One-dimensional numerical modeling of laser-matter interactions predicts the increase in both the mean and maximum energy of generated fast electrons with increased preformed plasma scale lengths for the range of laser intensities 10^{19}–10^{21} W cm^{-2}. The stochastic heating of electrons due to counterpropagating EM waves (incident and reflected waves) is found to be the dominant preformed plasma heating mechanism. The longitudinal electrostatic potential well, developed self-consistently in the preformed plasma, plays a crucial role in the further heating of the electrons. The constant push in one direction by this longitudinal electric field causes a reduction in the phase slip between the electron and one of the EM waves. This finally results in higher-energy gains by the locking of the electron with one of the two EM waves. This is found to be the underlying physics behind the higher-energy gain in the presence of a longitudinal electric field. The extent of the potential well is decided by the preformed plasma scale length. The potential well gets wider with an increase in the preformed plasma scale length, thereby causing extension of the phase-space mixing region. This explains the stronger heating and higher mean energy of generated fast electrons in the presence of a larger preformed plasma scale length. The electrons contributing to the high-energy tail of the spectrum come from the underdense region of preformed plasma. These electrons, after getting locked with the forward-going EM wave, gain more energy due to longer interaction time (and distance) with the wave. This explains the increase in maximum energy of electrons with the increasing preformed plasma scale length.

The effect of ion motion is studied by performing separate simulations with mobile ions. The ions respond to the longitudinal electric potential produced due to plasma electrons heating, which results in the steepening of the plasma profile near the critical density surface (generally referred to as ponderomotive steepening). The expansion of the low-density shelf towards the vacuum causes the extension of the region of phase-space mixing. Therefore, significantly higher absorption is found in the mobile ion simulations compared to the immobile ion simulations.

The multidimensional effects of laser propagation through underdense plasmas such as filamentation, self-focusing, defocusing, etc., are neglected in the present 1D studies. Also, 1D representation cannot be applied when preformed plasma scale length becomes considerably larger than the laser spot size, which is typically 10–20 μm. Furthermore, it should be noted that results presented in this paper are mainly applicable in the preformed plasma scale length range of 1–15 μm, and different laser absorption and fast electrons energy coupling can be expected with much larger preformed plasma scale lengths (i.e., $L_p \to \infty$). The strong prepulse can damage the solid target. This may constrain the maximum preformed plasma scale length one can expect in the experiments. Finally, we would like to point out that, although we see an increase in fast electrons energy with increasing preformed plasma scale length, for applications such as fast ignition [1] large preformed plasma can be detrimental due to the shift of relativistic critical surface away from the core. We plan to address some these limitations of our present work, especially the multidimension effects, in future studies.

ACKNOWLEDGMENTS

This work is supported by the US Department of Energy under Contracts No. DE-FC02-04ER54789 (Fusion Science Center) and No. DE-FG-02-05ER54834 (ACE). We would like to thank Dr. Mike H. Key and Dr. Pravesh K. Patel from Lawrence Livermore National Laboratory for their useful discussions.

---

[1] M. Tabak, J. Hammer, M. E. Glinsky, W. L. Kruer, S. C. Wilks, J. Woodworth, E. M. Campbell, M. D. Perry, and R. J. Mason, Phys. Plasmas **1**, 1626 (1994).

[2] T. Tajima and J. M. Dawson, Phys. Rev. Lett. **43**, 267 (1979).

[3] S. C. Wilks, A. B. Langdon, T. E. Cowan, M. Roth, M. Singh, S. Hatchett, M. H. Key, D. Pennington, A. Mackinnon, and R. A. Snavely, Phys. Plasmas **8**, 542 (2001).

[4] E. P. Liang, S. C. Wilks, and M. Tabak, Phys. Rev. Lett. **81**, 4887 (1998).

[5] F. N. Beg, A. R. Bell, A. E. Dangor, C. N. Danson, A. P. Fews, M. E. Glinsky, B. A. Hammel, P. Lee, P. A. Norreys, and M. Tatarakis, Phys. Plasmas **4**, 447 (1997).

[6] S. C. Wilks, W. L. Kruer, M. Tabak, and A. B. Langdon, Phys. Rev. Lett. **69**, 1383 (1992).

[7] T. Yabuuchi, B. S. Paradkar, M. S. Wei, J. A. King, F. N. Beg, R. B. Stephens, N. Nakanni, H. Hatakeyama, H. Habara, K. Mima, K. A. Tanaka, and J. T. Larsen, Phys. Plasmas **17**, 060704 (2010).

[8] A. G. MacPhee, L. Divol, A. J. Kemp, K. U. Akli, F. N. Beg, C. D. Chen, H. Chen, D. S. Hey, R. J. Fedosejevs, R. P. Freeman, M. Henesian, M. H. Key, S. Le Pape, A. Link, T. Ma, A. J. Mackinnon, V. M. Ovchinnikov, P. K. Patel, T. W. Phillips, R. B. Stephens, M. Tabak, R. Town, Y. Y. Tsui, L. D. Van Woerkom, M. S. Wei, and S. C. Wilks, Phys. Rev. Lett. **104**, 055002 (2010).

[9] A. J. Kemp, Y. Sentoku, and M. Tabak, Phys. Rev. E **79**, 066406 (2009).

[10] H. Cai, K. Mima, A. Sunahara, T. Johzaki, H. Nagatomo, S. Zhu, and X. T. He, Phys. Plasmas **17**, 023106 (2010).

[11] M. Sherlock, Phys. Plasmas **16**, 103101 (2009).

[12] A. Pukhov, Z. M. Sheng, and J. Meyer-ter-vehn, Phys. Plasmas **6**, 2847 (1999).

[13] E. Lefebvre and G. Bonnaud, Phys. Rev. E **55**, 1011 (1997).

[14] G. Sun, Ott E, Y. Lee, and P. Guzdar, Phys. Fluids **30**, 526 (1987).

[15] C. E. Max, J. Arons, and A. B. Langdon, Phys. Rev. Lett. **33**, 209 (1974).

[16] D. R. Welch, D. V. Rose, M. E. Cuneo, R. B. Campbell, and T. A. Mehlhorn, Phys. Plasmas **13** 063105 (2006).

[17] D. R. Welch, D. V. Rose, B. V. Oliver, and R. E. Clark, Nucl. Instrum. Methods Phys. Res. A **464**, 134 (2001).

[18] H. Chen and S. C. Wilks, Laser and Particle Beams **23**, 411 (2005).

[19] J. D. Lawson, IEE Trans. Nucl. Sci. **26**, 4217 (1979).

[20] W. Kruer, *The Physics of Laser Plasma Interactions* (Addison-Wesley, Reading, MA, 1988), Chap. 5.

[21] W. L. Kruer and K. Estrabook, Phys. Fluids **28**, 430 (1985).

[22] Z. M. Sheng, K. Mima, J. Zhang, and J. Meyer-ter-Vehn, Phys. Rev. E **69**, 016407 (2004).

[23] A. Bourdier, D. Patin, and E. Lefebvre, Laser Part. Beams **25**, 169 (2007).

[24] C. K. Birdsall and A. B. Langdon, *Plasma Physics via Computer Simulations* (McGraw-Hill, New York, 1985).